

Article

Position and Speed Estimation of Permanent Magnet Machine Sensorless Drive at High Speed Using an Improved Phase-Locked Loop

Guan-Ren Chen ¹, Shih-Chin Yang ^{1,*}, Yu-Liang Hsu ²  and Kang Li ¹ 

¹ Department of Mechanical Engineering, National Taiwan University, No. 1, Sec. 4, Roosevelt Road, Taipei 10617, Taiwan; d03522014@ntu.edu.tw (G.-R.C.); kangli@ntu.edu.tw (K.L.)

² Department of Automatic Control Engineering, Feng Chia University, No. 100 Wenhwa Road, Taichung 40724, Taiwan; hsuy1@fcu.edu.tw

* Correspondence: scy99@ntu.edu.tw

Received: 4 September 2017; Accepted: 27 September 2017; Published: 11 October 2017

Abstract: In conventional position sensorless permanent magnet (PM) machine drives, the rotor position is obtained from the phase-locked loop (PLL) with the regulation of spatial signal in estimated back electromotive force (EMF) voltages. Due to the sinusoidal distribution of back-EMF voltages, a small-signal approximation is assumed in the PLL in order to estimate the position. That is, the estimated position is almost equal to the actual position per sample instant. However, at high speed when the ratio of sampling frequency, f_{sample} , over the rotor operating frequency, f_e , is low, this approximation might not be valid during the speed and load transient. To overcome this limitation, a position estimation is proposed specifically for the high-speed operation of a PM machine drive. A discrete-time EMF voltage estimator is developed to obtain the machine spatial signal. In addition, an arctangent calculation is cascaded to the PLL in order to remove this small-signal approximation for better sensorless drive performance. By using the discrete-time EMF estimation and modified PLL, the drive is able to maintain the speed closed-loop at 36 krpm with only 4.2 sampling points per electrical cycle on a PM machine, according to experimental results.

Keywords: motor drives; position sensorless drive; back EMF estimation

1. Introduction

Permanent magnet (PM) machines are widely used in motion applications with high power densities, e.g., pumps, compressors and fans. In particular, PM machine drives at high speed have demonstrated advantages in applications with a size constraint [1–3]. Among these applications, machine drives without position sensors are preferred, since the sensor installation reduces the torque density per unit volume and increases the overall drive size [4–6]. To reduce the cost and volume of the device, a single current sensor drive is proposed in [7] which can reconstruct three phase currents based on the measurement of DC-link current. In [8], several sensorless drives for PM machines have been reviewed. By using the spatial signal in the machine itself, position sensorless drives are able to perform field-oriented control (FOC) without separate position sensors [8–10].

Position sensorless drives can be categorized as saliency-based drives [11,12] and electromotive force (EMF) based drives [13–18] dependent on the spatial signal in a machine. For operation at zero and low speed, position estimation using the spatial signal in rotor saliencies is preferred because all EMF-based drives eventually fail at very low speed [11,12,19]. Reference [17] proposed an improved initial rotor position estimation for low-salient machines. By contrast with conventional methods, polarity detection is more accurate, by filtering the spatial harmonics in inductances. In addition, [20] addresses the sensorless estimation of interior PM machines using rotor saliency and the adaptive filter.

The position signal is obtained directly from current ripples instead of saliency signal demodulation. It can be concluded that the signal is better due to the adjustable controller bandwidth. By contrast, beyond 10% rated speed position estimation using the spatial signal in EMF voltages results in a comparable performance to saliency-based drives [14,15,20]. Under this effect, EMF-based position estimation methods are preferred at high speed for the sensorless drive, because no voltage injection is required to fully utilize the DC bus voltage.

For EMF-based drives, the EMF voltage is estimated according to the voltage and current relationship with the knowledge of machine resistance and inductance. The rotor position is then calculated by obtaining the spatial signal in the estimated EMF voltage. The overall EMF-based drive system is shown in Figure 1. Considering the EMF estimation algorithm denoted by the blue block, EMF voltage can be estimated from either the open-loop calculation based on the machine model [14,21–25] or the closed-loop state estimation using observer technologies [26–32]. Open-loop methods directly calculate EMF voltage based on the machine model. The estimation accuracy can be influenced by current noises as well as resistance and inductance variation due to the open-loop calculation. By contrast, closed-loop methods estimate EMF using the current observer with machine parameters. Because of the observer filter property, the influence of current noises can be negligible. Reference [18] improves the conventional observer estimation by compensating the DC offset error resulting from the A/D converter, op-amp gain and voltage sensor gain deviation. A nonlinear PLL is also added to improve the observer estimation performance [33]. A speed controller is also proposed to achieve a better sensorless dynamic performance. Reference [34] proposed an active damping control for the sensorless drive of an interior PM machine. The proposed method reduces the influence of parameter errors by increasing the equivalent damping of the drive system. In addition, [35] developed an adaptive torque estimation for PM machines considering the inductance parameter variation. However, the accuracy of EMF estimation is still sensitive to the parameter variation. It is also noteworthy that the observer estimation bandwidth strongly depends on the signal-to-noise ratio of machine currents. At high speed, due to the limited bandwidth, EMF estimation in the observer might result in phase lag, which degrades the sensorless drive performance.

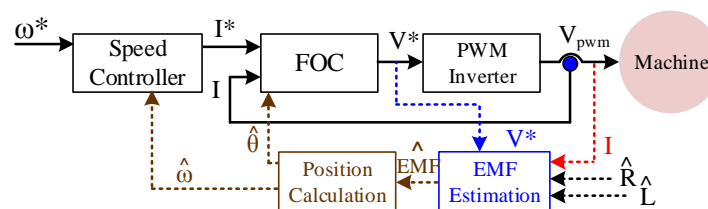


Figure 1. Illustration of electromotive force (EMF) based position sensorless drive system.

EMF voltages can be estimated based on AC signals in the stator-referred stationary frame [26,27] or DC signals in the rotor synchronous frame [28,29]. For AC EMF voltages, the rotor position is calculated based on the arctangent function [27] or the PLL [20,26,33]. On the other hand, for DC EMF voltages, the rotor position can only be obtained from the PLL. Considering the position estimation using PLL, a small-signal approximation is assumed where the estimated position $\hat{\theta}_e$ is almost equal to the actual position θ_e . Under this effect, the feedback position signal $\sin(\theta_e - \hat{\theta}_e)$ can be simplified by $\theta_e - \hat{\theta}_e$ for the closed-loop regulation [9,10,13,36]. Unfortunately, at high speed, the ratio of sampling frequency, f_{sample} , over the rotor operating frequency, f_e , is low due to the limitation on the inverter switching frequency. Considering the discretized effect at low f_{sample}/f_e , the assumption where $\sin(\theta_e - \hat{\theta}_e) \approx \theta_e - \hat{\theta}_e$ might not be valid, leading to stability issues on EMF-based drives.

This paper improves the PM machine sensorless drive specifically for high-speed operation. As reported in [37], a discrete-time machine model is implemented to estimate EMF voltages considering discretized effects at low f_{sample}/f_e . The high-speed drive performance can be improved by including the zero-order-hold (ZOH) reflected voltage delay in the EMF estimation. This paper

extends [37] in order to further enhance the sensorless position estimation using discretized EMF voltages. On that basis, a PLL cascaded with an arctangent function is used to remove the small-signal approximation at high speed. By using the arctangent calculation, the dynamic operation of a sensorless drive can be maintained even at high speed with low f_{sample}/f_e . By cascading the PLL after the arctangent calculation, the position estimation error is reduced due to the filter property in the PLL [20,33]. In addition, compared to existing estimation methods receiving only the spatial signal from d-axis EMF [9,10,13,36], the proposed position estimation uses spatial signals from both the d- and q-axis EMF voltage. At high speed, another advantage is the reduced parameter sensitivity on the EMF-based position estimation. In this paper, a 126-W 8-pole surface PM machine is experimentally tested. By applying the discrete-time EMF estimation and modified PLL, the drive can operate at the speed of 36 krpm under 50% step load with only 4.2 sampling points per electrical cycle, where $f_e = 2.4$ -kHz, $f_{sample} = 10$ -kHz and $f_{sample}/f_e = 4.2$.

2. Discrete-Time EMF Estimation

This section explains the discrete-time EMF estimation used for the position and speed calculation. As seen for the overall sensorless drive signal flowchart in Figure 1, this EMF estimation is equivalent to the blue box. Considering firstly the continuous-time system, the machine model can be shown by (1) in $\alpha\beta$ stator-referred stationary frame.

$$V_{\alpha\beta}(t) = R_s I_{\alpha\beta}(t) + L_s \frac{d}{dt} I_{\alpha\beta}(t) + E_{\alpha\beta}(t) \quad (1)$$

where the subscript $\alpha\beta$ represents the complex vector, $F_{\alpha\beta} = f_\alpha + jf_\beta$, in the stator frame; $V_{\alpha\beta}(t)$ and $I_{\alpha\beta}(t)$ are continuous stator $\alpha\beta$ voltages and currents; R_s and L_s are the phase resistance and inductance; and $E_{\alpha\beta}(t)$ are continuous $\alpha\beta$ EMF voltages. In this paper, a constant phase inductance is assumed for simplicity. The influence of inductance variation on the discrete-time EMF estimation has been analyzed in [36].

For machine drives with embedded controllers, a zero-order-hold should be implemented to convert discrete-time voltages to pulse width modulation (PWM) voltages. Considering the influence of ZOH, the relationship between continuous $V_{\alpha\beta}(t)$ and discretized $V_{\alpha\beta}(kT)$ is shown by:

$$V_{\alpha\beta}(t) = V_{\alpha\beta}(kT) \quad \text{when } kT < t < (K + 1)T \quad (2)$$

where T and k are the sampling time and sequence, respectively. By solving the differential equation in (1) with the discrete-time voltage inputs, $V_{\alpha\beta}(kT)$ in (2), the discrete-time machine model can be obtained by (3) [37].

$$I_{\alpha\beta}(kT) = e^{-\frac{R_s}{L_s}T} I_{\alpha\beta}[(k-1)T] + \frac{1 - e^{-\frac{R_s}{L_s}T}}{R_s} V_{\alpha\beta}[(k-1)T] - \frac{e^{j\omega_e T} - e^{-\frac{R_s}{L_s}T}}{R_s + j\omega_e L_s} E_{\alpha\beta}[(k-1)T] \quad (3)$$

where ω_e is the rotor speed. (3) derives the model in the stator frame with inputs of discrete-time voltage command, $V_{\alpha\beta}(kT)$, and outputs of sampled currents, $I_{\alpha\beta}(kT)$. Considering the sensorless drive at high speed, EMF estimation in the rotor frame is preferred, since the estimation bandwidth is greatly increased by regulating dq EMF voltages with DC signals. As a result, the discrete-time machine model in the rotor frame is developed based on the frame transformation.

$$\begin{aligned} I_{dq}(kT) &= I_{\alpha\beta}(kT) e^{-j\theta_e(kT)} \\ &= e^{-\frac{R_s}{L_s}T} I_{\alpha\beta}[(k-1)T] e^{-j\theta_e(kT)} + \frac{1 - e^{-\frac{R_s}{L_s}T}}{R_s} V_{\alpha\beta}[(k-1)T] e^{-j\theta_e(kT)} - \frac{e^{j\omega_e T} - e^{-\frac{R_s}{L_s}T}}{R_s + j\omega_e L_s} E_{\alpha\beta}[(k-1)T] e^{-j\theta_e(kT)} \end{aligned} \quad (4)$$

where θ_e is the rotor position. In (4), the current step of position $\theta_e(kT)$ can be formulated by the last step of position $\theta_e[(k-1)T]$ and the speed, ω_e , which is given by:

$$\theta_e(kT) = \theta_e[(k-1)T] + \omega_e T \quad (5)$$

Based on (5), the last step of $\alpha\beta$ currents $I_{\alpha\beta}[(k-1)T]$, voltages $V_{\alpha\beta}[(k-1)T]$ and EMF $E_{\alpha\beta}[(k-1)T]$, can convert to dq variables, $I_{dq}[(k-1)T]$, $V_{dq}[(k-1)T]$ and $E_{dq}[(k-1)T]$, by multiplying $e^{-j\theta_e}(kT)$ to $I_{\alpha\beta}[(k-1)T]$, $V_{\alpha\beta}[(k-1)T]$ and $E_{\alpha\beta}[(k-1)T]$. They are respectively shown by:

$$I_{\alpha\beta}[(k-1)T]e^{-j\theta_e(kT)} = I_{\alpha\beta}[(k-1)T] \left[e^{-j\theta_e[(k-1)T]} \times e^{-j\omega_e T} \right] = \left[I_{\alpha\beta}[(k-1)T] \times e^{-j\theta_e[(k-1)T]} \right] e^{-j\omega_e T} \tag{6}$$

$$= I_{dq}[(k-1)T]e^{-j\omega_e T}$$

$$V_{\alpha\beta}[(k-1)T]e^{-j\theta_e(kT)} = V_{dq}[(k-1)T]e^{-j\omega_e T} \tag{7}$$

$$E_{\alpha\beta}[(k-1)T]e^{-j\theta_e(kT)} = E_{dq}[(k-1)T]e^{-j\omega_e T} \tag{8}$$

By substituting (6)–(8) into (4), the discrete-time machine model in the rotor frame is obtained by (9).

$$I_{dq}(kT) = e^{-\frac{R_s}{L_s}T - j\omega_e T} I_{dq}[(k-1)T] + \frac{e^{-j\omega_e T} - e^{-\frac{R_s}{L_s}T - j\omega_e T}}{R_s} V_{dq}[(k-1)T] - \frac{1 - e^{-\frac{R_s}{L_s}T - j\omega_e T}}{R_s + j\omega_e L_s} E_{dq}[(k-1)T] \tag{9}$$

(9) shows the discrete-time machine model using the complex vector. The actual discrete-time response of both $i_d(kT)$ and $i_q(kT)$ can be demonstrated easily using the state space equation, which is given by

$$\begin{bmatrix} i_d(kT) \\ i_q(kT) \end{bmatrix} = G \begin{bmatrix} \cos(\omega_e T) & -\sin(\omega_e T) \\ \sin(\omega_e T) & \cos(\omega_e T) \end{bmatrix} \begin{bmatrix} i_d[(k-1)T] \\ i_q[(k-1)T] \end{bmatrix} + \begin{bmatrix} F & 0 \\ 0 & F \end{bmatrix} \begin{bmatrix} v_d[(k-1)T] \\ v_q[(k-1)T] \end{bmatrix} - \frac{1}{R_s^2 + \omega_e^2 L_s^2} \begin{bmatrix} EMF_1 & -EMF_2 \\ EMF_2 & EMF_1 \end{bmatrix} \begin{bmatrix} e_d[(k-1)T] \\ e_q[(k-1)T] \end{bmatrix} \tag{10}$$

where the variables F , G , EMF_1 and EMF_2 are defined by (11)–(13) to simplify the equation in (10).

$$F = \frac{1 - e^{-\frac{R_s}{L_s}T}}{R_s} \text{ and } G = e^{-\frac{R_s}{L_s}T} \tag{11}$$

$$EMF_1 = R_s[1 - G \cos(\omega_e T)] + \omega_e L_s G \sin(\omega_e T) \tag{12}$$

$$EMF_2 = R_s G \sin(\omega_e T) - \omega_e L_s [1 - G \cos(\omega_e T)] \tag{13}$$

Figure 2 illustrates the corresponding discrete-time machine model with inputs of $V_{dq}(kT)$, outputs of $I_{dq}(kT)$ and disturbances of $E_{dq}(kT)$. It is observed that a phase advanced term, $e^{-j\omega_e T}$, appears in dq currents, voltages and EMF. According to the discrete-time model in (10), EMF voltages in the rotor frame can be directly calculated based on the relationship between $V_{dq}(kT)$ and $I_{dq}(kT)$ in Figure 2 with the knowledge of \hat{R}_s and \hat{L}_s . It is shown to be:

$$\begin{bmatrix} e_d[(k-1)T] \\ e_q[(k-1)T] \end{bmatrix} = (\hat{R}_s^2 + \omega_e^2 \hat{L}_s^2) \begin{bmatrix} EMF_1 & -EMF_2 \\ EMF_2 & EMF_1 \end{bmatrix}^{-1} \left\{ \begin{bmatrix} \cos(\hat{\omega}_e T) & -\sin(\hat{\omega}_e T) \\ \sin(\hat{\omega}_e T) & \cos(\hat{\omega}_e T) \end{bmatrix} \begin{bmatrix} \hat{F} & 0 \\ 0 & \hat{F} \end{bmatrix} \begin{bmatrix} v_d[(k-1)T] \\ v_q[(k-1)T] \end{bmatrix} - \begin{bmatrix} i_d(kT) \\ i_q(kT) \end{bmatrix} + \hat{G} \begin{bmatrix} \cos(\hat{\omega}_e T) & -\sin(\hat{\omega}_e T) \\ \sin(\hat{\omega}_e T) & \cos(\hat{\omega}_e T) \end{bmatrix} \begin{bmatrix} i_d[(k-1)T] \\ i_q[(k-1)T] \end{bmatrix} \right\} \tag{14}$$

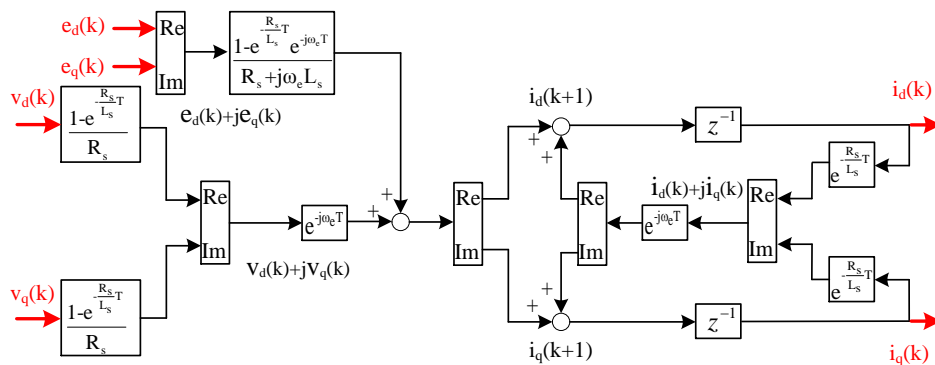


Figure 2. The discrete-time machine model in the rotor-referred synchronous frame.

In (14), $\hat{E}_{dq}(kT)$ represents the estimated dq EMF voltages, and $\hat{\omega}_e$ is the estimated speed. In addition, \hat{F} , \hat{G} , \hat{EMF}_1 and \hat{EMF}_2 are calculated using the knowledge of \hat{R}_s , \hat{L}_s and $\hat{\omega}_e$. In this paper, \hat{R}_s and \hat{L}_s are measured from a RLC meter offline. It can be noted that the open-loop EMF estimation in (14) is applied to obtain $\hat{E}_{dq}(kT)$. Because of open-loop estimation, $\hat{E}_{dq}(kT)$ might be sensitive to the noises in $I_{dq}(kT)$. However, for the high-speed operation, the magnitude of $\hat{E}_{dq}(kT)$ is sufficiently higher than the resistance reflected voltage drop. In addition, as reported in [30], the observer-based estimation might cause the phase lag in $\hat{E}_{dq}(kT)$ due to the limited observer bandwidth at high speed. Considering this delay issue, the direct EMF calculation is implemented for the high-speed sensorless drive with low f_{sample}/f_e .

It is important that the proposed discrete-time EMF estimation in (14) is substantially different to conventional continuous-time models in [13–16]. In particular, $e^{-j\omega_e T}$ is resultant due to the influence of ZOH, as seen in Figure 2. As speed increases, the percentage of $e^{-j\omega_e T}$ on $\hat{E}_{dq}(kT)$ increases, leading to additional estimation errors. Under this effect, the EMF estimation in (14) including the ZOH effect is suited for the sensorless drive at high speed.

Considering a perfect parameter estimation, the estimated dq EMF voltages $\hat{E}_{dq}(kT)$ should be equal to actual EMF $E_{dq}(kT)$, which is given by:

$$\hat{E}_{dq}(kT) = \begin{bmatrix} \hat{e}_d(kT) \\ \hat{e}_q(kT) \end{bmatrix} = E_{dq}(kT) = \begin{bmatrix} e_d(kT) \\ e_q(kT) \end{bmatrix} = \begin{bmatrix} 0 \\ \omega_e(kT) \lambda_{pm} \end{bmatrix} \quad (15)$$

where $\omega_e(kT)$ and λ_{pm} are the actual rotor speed and magnet flux. It is important that in (15), $e_d(kT)$ should be zero, assuming the estimated position $\hat{\theta}_e$ is equal to the actual position θ_e . For the sensorless drive at the initial state, the rotor position might be unknown before signal processing of the position estimation. Under this effect, there is a position error, θ_{err} , between the estimated dq rotor frame and actual rotor frame, as seen in Figure 3 where $\theta_{err}(kT) = \theta_e(kT) - \hat{\theta}_e(kT)$. The subscripts, e' and e , represent the estimated and actual rotor frame. Since the estimated $\hat{E}_{dq}(kT)$ is initially located at the estimated frame, $\hat{E}_{dq}(kT)$ should be modulated by sinusoidal functions dependent on the magnitude of $\theta_{err}(kT)$, which is shown to be:

$$\hat{E}_{dq}(kT) = \begin{bmatrix} \hat{e}_d(kT) \\ \hat{e}_q(kT) \end{bmatrix} = \begin{bmatrix} -\omega_e(kT) \lambda_{pm} \sin[\theta_{err}(kT)] \\ \omega_e(kT) \lambda_{pm} \cos[\theta_{err}(kT)] \end{bmatrix} \quad (16)$$

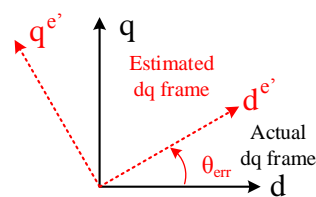


Figure 3. Illustration of estimated dq rotor frame to the actual dq rotor frame.

For the purpose of the sensorless drive, the actual position $\theta_e(kT)$ can be obtained by manipulating $\theta_{err}(kT)$ to be zero. Detailed position estimation processing will be explained in the next section.

3. Position Estimation at High Speed

This section analyzes the position calculation using the spatial signal from estimated $\hat{E}_{dq}(kT)$. For the overall sensorless drive system, the corresponding signal process is implemented in the brown box of Figure 1. On that basis, a PLL is developed to estimate the rotor speed $\hat{\omega}_e(kT)$ and position

$\hat{\theta}_e(kT)$ with the position error, $\theta_{err}(kT)$ in estimated EMF. As seen in (16), $\theta_{err}(kT)$ can be extracted using either the small-signal approximation in (17) or the arctangent function in (18).

$$\hat{e}_d(kT) = -\omega_e(kT) \lambda_{pm} \sin[\theta_{err}(kT)] \approx -\omega_e(kT) \lambda_{pm} \theta_{err}(kT) \quad (17)$$

$$\tan^{-1}\left(-\frac{\hat{e}_d(kT)}{\hat{e}_q(kT)}\right) = \tan^{-1}\left(\frac{\omega_e(kT) \lambda_{pm} \sin[\theta_{err}(kT)]}{\omega_e(kT) \lambda_{pm} \cos[\theta_{err}(kT)]}\right) = \theta_{err}(kT) \quad (18)$$

In (17), a small-signal approximation, where $\theta_{err}(kT) = \theta_e(kT) - \hat{\theta}_e(kT)$, is assumed to simplify the nonlinear sinusoidal function in $\hat{e}_d(kT)$. As illustrated in Figure 4a, a PLL with a proportional gain K_p and an integral gain K_i is applied to estimate $\hat{\omega}_e(kT)$ and $\hat{\theta}_e(kT)$ by manipulating $\hat{e}_d(kT)$ to be zero. A backward approximation is implemented for the discrete-time integration in Figure 4. In general, K_p determines the estimation bandwidth of PLL. If considerable harmonics are observed in $\hat{e}_d(kT)$, K_p should decrease to reduce the error on $\hat{\theta}_e(kT)$ and $\hat{\omega}_e(kT)$. On the other hand, the steady state error might occur on $\hat{\theta}_e(kT)$. This steady state estimation error can be removed by adding K_i . By properly assigning K_p and K_i simultaneously, the overall transfer function between $\hat{\theta}_e(kT)$ and $\hat{e}_d(kT)$ can be formulated as a second-order low-pass filter to improve estimation performance.

On the other hand, Figure 4b proposes a position estimation by adding an arctangent function in (18) cascaded to the same PLL. Due to the arctangent calculation, the small-signal approximation in (17) can be removed. At high speed, it will be demonstrated that the position estimation using the proposed PLL in Figure 4b achieves better drive performance for the following three reasons.

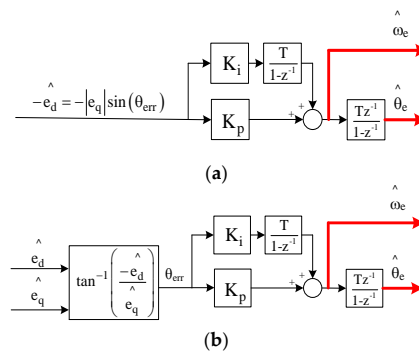


Figure 4. Position and speed estimation by regulating feedback position error signals of (a) the speed-dependent voltage error $\hat{e}_d(kT)$ and (b) the actual $\theta_{err}(kT)$ based on the arctangent calculation.

3.1. Unit Length Feedback Signal

For the position estimation in Figure 4a, the magnitude of $\hat{e}_d(kT)$ is proportional to $\lambda_{pm} \times \omega_e(kT)$, which is a speed-dependent signal. Under this effect, the speed-dependent estimation performance is resultant on $\hat{\theta}_e(kT)$. As reported in [38], the PLL might have a stability issue at low speed when $\hat{\omega}_e(kT) \approx 0$ due to the low magnitude of $\hat{e}_d(kT)$. Besides, at high speed the magnitude of $\hat{e}_d(kT)$ could be sufficient high. With the same K_p and K_i in Figure 4, high-frequency noises in $\hat{e}_d(kT)$ might increase, leading to considerable position errors at high speed.

For the proposed estimation in Figure 4b, a position error, $\hat{\theta}_e(kT)$, with a unit length is extracted using the arctangent calculation. The speed-dependent term is removed, since both $\hat{e}_d(kT)$ and $\hat{e}_q(kT)$ contain the same value in any operating conditions. Compared to Figure 4a, better position estimation performance based on Figure 4b can be achieved.

3.2. Increased Dynamic Response

In addition to speed-dependent estimation bandwidth, the PLL structure in Figure 4 also results in the discretized effect at high speed. Considering the low ratio of f_{sample}/f_e , the assumption

of $\theta_{err}(kT) = \theta_e(kT) - \hat{\theta}_e(kT) \approx 0$ might not be valid for the position estimation. For example, when $f_{sample} = 10\text{-kHz}$, $f_e = 1.67\text{-kHz}$ and $f_{sample}/f_e = 6$, the position calculation period in the microcontroller is every 60° per electrical cycle. At this time, the resolution of $\sin[\theta_{err}(kT)]$ is $\sin(60^\circ) = 0.866$, which might not be close to zero.

In order to analyze the accuracy of small-signal approximation in Figure 4a, the nonlinear equation in (17) is linearized at two different operating points, θ_e and $\hat{\theta}_e$, to obtain an analytical model. On that basis, the partial derivatives of both θ_e and $\hat{\theta}_e$ on $\sin(\theta_e - \hat{\theta}_e)$ are applied, which are respectively shown to be

$$\left. \frac{\partial \hat{e}_d}{\partial \theta_e} \right|_{\substack{\theta_e = \theta_{e0} \\ \hat{\theta}_e = \hat{\theta}_{e0}}} = \left. \frac{\partial |e_q|}{\partial \theta_e} \sin(\theta_e - \hat{\theta}_e) \right|_{\substack{\theta_e = \theta_{e0} \\ \hat{\theta}_e = \hat{\theta}_{e0}}} = |e_q| \cos(\theta_{e0} - \hat{\theta}_{e0}) \tag{19}$$

$$\left. \frac{\partial \hat{e}_d}{\partial \hat{\theta}_e} \right|_{\substack{\theta_e = \theta_{e0} \\ \hat{\theta}_e = \hat{\theta}_{e0}}} = \left. \frac{\partial |e_q|}{\partial \hat{\theta}_e} \sin(\theta_e - \hat{\theta}_e) \right|_{\substack{\theta_e = \theta_{e0} \\ \hat{\theta}_e = \hat{\theta}_{e0}}} = -|e_q| \cos(\theta_{e0} - \hat{\theta}_{e0}) \tag{20}$$

where θ_{e0} and $\hat{\theta}_{e0}$ are the equivalent points with respect to θ_e and $\hat{\theta}_e$. According to (19) and (20), the nonlinear PLL in Figure 4a can be linearized by Figure 5 at different operating points, θ_{e0} and $\hat{\theta}_{e0}$.

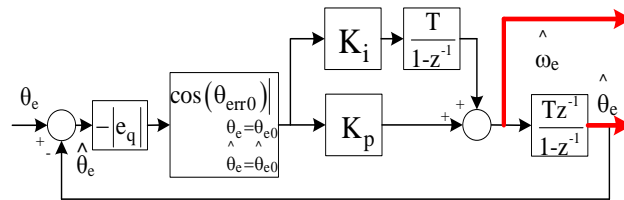


Figure 5. Position and speed estimation based on the PLL with the operating point model at $\theta_e = \theta_{e0}$ and $\hat{\theta}_e = \hat{\theta}_{e0}$.

Figure 6 further compares the feedback spatial signals between $\theta_{err}(kT)$ from the arctangent calculation in (18) and $\sin[\theta_{err}(kT)]$ based on the approximation in (17). The horizontal axis of actual θ_{err} is used to analyze the error under these two different signal processes. Ideally, the value in the vertical axis should be equal to that in the horizontal axis as the actual θ_{err} changes to the zero position error. It is shown that $\theta_{err}(kT)$ obtained in (18) increases linearly as actual θ_{err} increases. The PLL estimation stability can be maintained up to actual $\theta_{err} = 180^\circ$. On the other hand, $\sin[\theta_{err}(kT)]$, based on (17), results in the unstable PLL estimation when actual θ_{err} is beyond 90° due to the negative slope. More importantly, even in the stable region the deviation between $\sin[\theta_{err}(kT)]$ and $\theta_{err}(kT)$ significantly increases when actual θ_{err} reaches 60° . Considering the dynamic operation at high speed, $\theta_{err}(kT) = \theta_e(kT) - \hat{\theta}_e(kT)$ cannot be maintained at zero during the speed and load transient. Degraded drive performance must result, due to the approximation error shown in Figure 6.

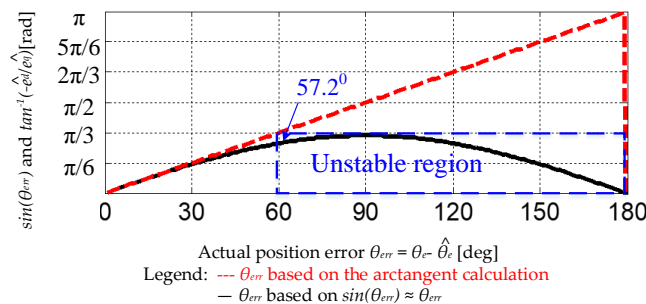


Figure 6. Feedback position signal $\sin(\theta_{err})$ in Figure 4a and θ_{err} in Figure 4b as the actual θ_{err} changes from $0\text{--}180^\circ$ (simulation results and $1\pi \text{ rad} = 180^\circ$).

Figure 7 shows the simulation results of (a) feedback spatial signals, the normalized $-\hat{e}_{d-pu}(kT)$ and $\tan^{-1}[-\hat{e}_d(kT)/\hat{e}_q(kT)]$, and (b) the estimated rotor frequency \hat{f}_e versus time. In this simulation, the speed-dependent component $|e_q|$ in $\hat{e}_d(kT)$ of (17) is removed to obtain the normalized $-\hat{e}_{d-pu}(kT)$ in order to easily compare the result using $\tan^{-1}[-\hat{e}_d(kT)/\hat{e}_q(kT)]$. The rotor frequency f_e is controlled to increase from 0–2.5 kHz (f_{sample}/f_e decreases from ∞ to 4). The acceleration rate is 3 kHz/s to analyze the limitation in (16) under the dynamic operation. In this case, $-\hat{e}_d(kT)$ and $\tan^{-1}[-\hat{e}_d(kT)/\hat{e}_q(kT)]$ in (a) all contain a certain amount of error due to the rapid acceleration. However, when \hat{f}_e is close to 1.5 kHz, the feedback signal, $-\hat{e}_{d-pu}(kT) = \sin[\theta_{err}(kT)]$, reaches 1, leading to the positive feedback in PLL, as illustrated in Figure 8. A considerable oscillation on f_e is then induced, where $-\hat{e}_{d-pu}(kT)$ varies between -1 and 1 . Based on this simulation, the PLL estimation in Figure 4a loses the stability when $-\hat{e}_{d-pu}(kT) \geq 1$. On the contrary, due to the linear relationship between $\tan^{-1}[-\hat{e}_d(kT)/\hat{e}_q(kT)]$ and actual θ_{err} , the PLL in Figure 4b performs well under this rapid acceleration.

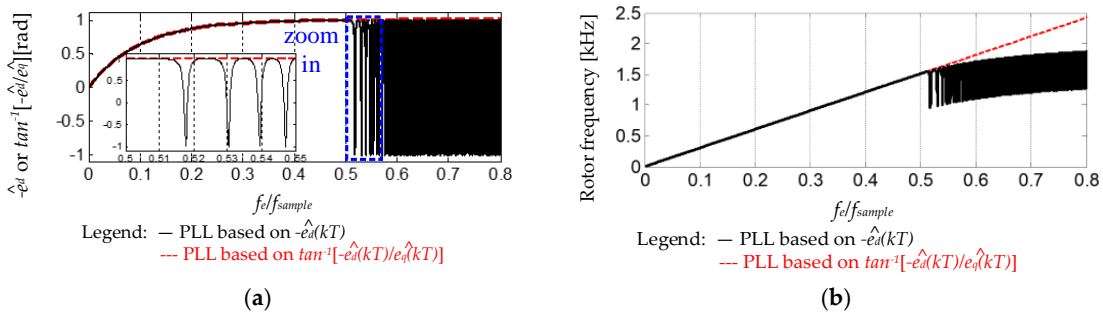


Figure 7. (a) Feedback $-\hat{e}_{d-pu}$ and $\tan^{-1}(-\hat{e}_d/\hat{e}_q)$ and (b) corresponding estimated rotor frequency \hat{f}_e versus time as the speed increases from 0 Hz to 2.5 kHz (simulation and f_{sample}/f_e from ∞ to 4).

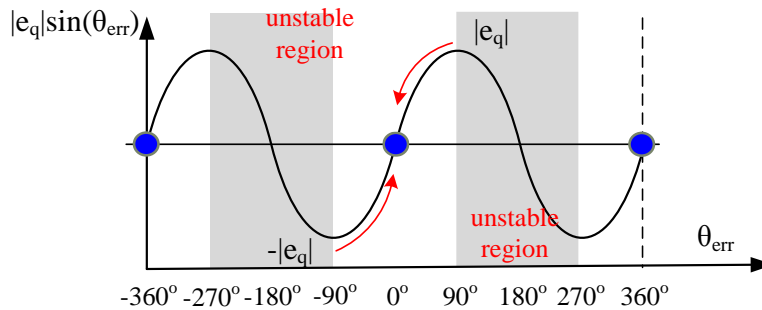


Figure 8. The estimated d-axis EMF voltage versus the position error from -360° to 360° .

3.3. Reduced Sensitivity on the Parameter Error

In addition to the improved dynamic operation, the PLL estimation in Figure 4b also achieves reduced sensitivity on the machine parameter variation compared to the estimation in Figure 4a. Considering the parameter error, the EMF estimation in (14) should be modified by

$$\begin{bmatrix} \hat{e}_{d-p}[(k-1)T] \\ \hat{e}_{q-p}[(k-1)T] \end{bmatrix} = \begin{bmatrix} \hat{e}_d[(k-1)T] \\ \hat{e}_q[(k-1)T] \end{bmatrix} + \begin{bmatrix} e_{d-Rerr}[(k-1)T] \\ e_{q-Rerr}[(k-1)T] \end{bmatrix} + \begin{bmatrix} e_{d-Lerr}[(k-1)T] \\ e_{q-Lerr}[(k-1)T] \end{bmatrix} \quad (21)$$

where $\hat{E}_{dq-p}(kT)$ are estimated EMF voltages with the parameter error, and $E_{dq-Rerr}(kT)$ and $E_{dq-Lerr}(kT)$ are additional components due to estimation errors from the resistance and inductance.

Assuming the resistance and inductance estimation error are $\Delta R_s = R_s - \hat{R}_s$ and $\Delta L_s = L_s - \hat{L}_s$, $E_{dq-Rerr}(kT)$ and $E_{dq-Lerr}(kT)$ can be obtained from (14), which are shown in (22) and (23), respectively.

$$\begin{bmatrix} e_{d-Rerr}[(k-1)T] \\ e_{q-Rerr}[(k-1)T] \end{bmatrix} = \begin{bmatrix} \Delta R_s & 0 \\ 0 & \Delta R_s \end{bmatrix} \left\{ \frac{1}{\Delta R_s^2} \begin{bmatrix} \cos(\hat{\omega}_e T) & -\sin(\hat{\omega}_e T) \\ \sin(\hat{\omega}_e T) & \cos(\hat{\omega}_e T) \end{bmatrix} \times \begin{bmatrix} v_d[(k-1)T] \\ v_q[(k-1)T] \end{bmatrix} - \begin{bmatrix} i_d(kT) \\ i_q(kT) \end{bmatrix} \right\} \quad (22)$$

$$\begin{bmatrix} e_{d-Lerr}[(k-1)T] \\ e_{q-Lerr}[(k-1)T] \end{bmatrix} = \Delta \omega_e^2 L_s^2 \begin{bmatrix} \Delta EMF_{Lerr1} & -\Delta EMF_{Lerr2} \\ -\Delta EMF_{Lerr2} & \Delta EMF_{Lerr1} \end{bmatrix}^{-1} \times \left\{ \frac{T^2}{\Delta L_s^2} \begin{bmatrix} \cos(\hat{\omega}_e T) & -\sin(\hat{\omega}_e T) \\ \sin(\hat{\omega}_e T) & \cos(\hat{\omega}_e T) \end{bmatrix} \begin{bmatrix} v_d[(k-1)T] \\ v_q[(k-1)T] \end{bmatrix} - \begin{bmatrix} i_d(kT) \\ i_q(kT) \end{bmatrix} + \begin{bmatrix} \cos(\hat{\omega}_e T) & -\sin(\hat{\omega}_e T) \\ \sin(\hat{\omega}_e T) & \cos(\hat{\omega}_e T) \end{bmatrix} \begin{bmatrix} i_d[(k-1)T] \\ i_q[(k-1)T] \end{bmatrix} \right\} \quad (23)$$

where

$$\Delta EMF_{Lerr1} = \Delta \omega_e L_s \sin(\omega_e T) \quad (24)$$

$$\Delta EMF_{Lerr2} = -\Delta \omega_e L_s [1 - \cos(\omega_e T)] \quad (25)$$

It is noteworthy that both (22) and (23) contain the $\hat{\omega}_e$ dependent term. Thus, ΔR_s and ΔL_s all cause speed-dependent errors in estimated $\hat{e}_d(kT)$ and $\hat{e}_q(kT)$ under the digital implementation. Figure 9 analyzes feedback signals of $-\hat{e}_d(kT)$ and $\tan^{-1}[-\hat{e}_d(kT)/\hat{e}_q(kT)]$ versus f_{sample}/f_e , considering the parameter estimation error. In this simulation, $\hat{e}_{d-p}(kT)$ and $\hat{e}_{q-p}(kT)$ in (21) are calculated by adding $E_{dq-Rerr}(kT)$ and $E_{dq-Lerr}(kT)$. As shown in (a), the error of ΔR_s results in $\hat{\omega}_e$ dependent error on $\hat{e}_d(kT)$, where the error increases as $\hat{\omega}_e$ increases. For the PLL estimation in Figure 4a, an increased error on $\hat{\theta}_e$ at high speed should appear, leading to the reduced torque output. By contrast, the PLL in Figure 4b based on $\tan^{-1}[-\hat{e}_d(kT)/\hat{e}_q(kT)]$ is immune to ΔR_s once f_{sample}/f_e is higher than 0.025. By obtaining $\theta_{err}(kT)$ in (18), the position estimation performance can be insensitive to ΔR_s at high speed.

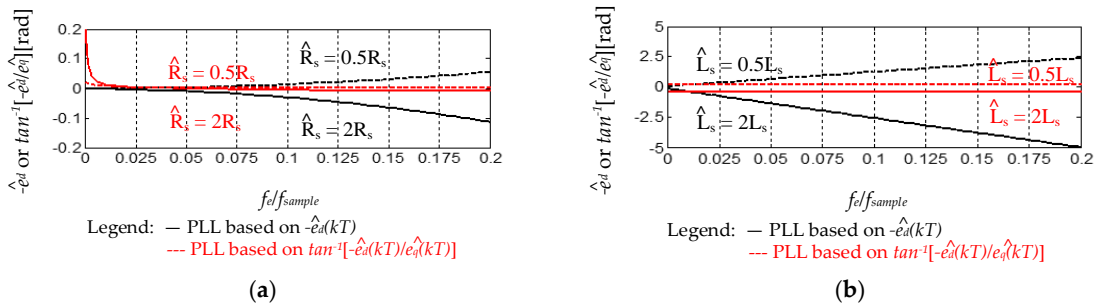


Figure 9. Feedback signal $-\hat{e}_d$ and $\tan^{-1}[-\hat{e}_d(kT)/\hat{e}_q(kT)]$ versus f_e/f_{sample} with the error of (a) resistance and (b) inductance (simulation result).

For the inductance variation in Figure 9b, $\hat{\omega}_e$ dependent error also appears in $\hat{e}_d(kT)$. More importantly, the error on $\hat{e}_d(kT)$ due to ΔL_s is significantly higher than that due to ΔR_s at high speed. Considering the inductance leakage effect and saturation at high speed, PLL estimation using only $\hat{e}_d(kT)$ can lead to a stability problem. On the contrary, a constant error on $\tan^{-1}[-\hat{e}_d(kT)/\hat{e}_q(kT)]$ is observed. The use of both d- and q-axis EMF voltages for the position estimation is the key for reducing the inductance variation at high speed with low f_e/f_{sample} . Based on this simulation, it is concluded that the reduced parameter sensitivity on the sensorless drive can be achieved using the proposed PLL estimation in Figure 4b. Table 1 lists the performance comparison between the PLL estimation in Figure 4a,b. Two advantages on the proposed PLL in (b) are summarized:

1. The dynamic response is improved at high speed. As seen for the feedback position error signal in Figure 7, the nonlinearity of $\sin(\theta_{err})$ appears once the position error between the estimated and actual position is higher than 57.2° . After adding the arctangent calculation, the signal of $\tan^{-1}(\hat{e}_d/\hat{e}_q)$ still maintains a linear waveform once the position error reaches 180° . Thus, a better estimation performance is achieved.

- The PLL cascaded the arctangent calculation also shows reduced sensitivity on the parameter variation at high speed. As seen in Figure 9, $\tan^{-1}(\hat{e}_d/\hat{e}_q)$ receives the position information from both $\hat{e}_d(kT)$ and $\hat{e}_q(kT)$. Compared to the conventional PLL obtaining the position information from only $\hat{e}_d(kT)$, it can be concluded that there is reduced sensitivity on the parameter. In addition, due to the reduced parameter sensitivity, the overall drive stability can also be improved using the proposed PLL.

Table 1. Comparison of two position estimation algorithms.

| Performance Index | Small-Signal in Figure 4a | Proposed PLL in Figure 4b |
|-----------------------------------|--|---------------------------|
| Transient response | Limited at high speed | Speed independent |
| Tolerance of position error | $\pm 2\pi/3$ | $\pm\pi$ |
| Steady state error | Degradation at high speed | Speed independent |
| Robustness of parameter variation | Degradation at high speed | Reduced effect |
| Controller delay | No difference (depends on the PLL bandwidth) | |
| Overall Stability | Normal | Better |

4. Experimental Results

An 8-pole surface PM machine with the rated speed of 12 krpm ($f_e = 0.8$ -kHz) was experimentally evaluated to verify the high-speed EMF-based sensorless drive using different PLL estimation structures. The test setup of the PM machine sensorless drive is shown in Figure 10. Table 2 lists key test machine and inverter characteristics. A hysteresis brake was back-to-back connected to the test machine for the load operation. Considering the switching loss and microcontroller bandwidth, the sampling frequency was selected at 10 kHz to synchronize with the PWM frequency. All sensorless drive algorithms in Figure 1 were implemented in a 32-bit microcontroller, TI-TMS320F28069 (Texas Instruments, Dallas, TX, USA). The estimated position and speed from Figure 4 were used for the speed control and FOC.

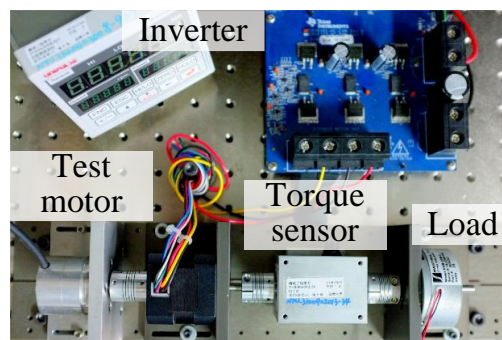


Figure 10. Test setup of PM machine sensorless drive.

Table 2. Test Machine Characteristics.

| Characteristics | Values |
|--------------------|---------------|
| Rotor poles | 8-pole |
| Rated torque | 0.1-Nm |
| Rated current | 1-A |
| Rated speed | 12-krpm |
| Resistance | 0.1- Ω |
| Inductance | 130- μ H |
| Sampling Frequency | 10-kHz |
| DC bus voltage | 48-V |

4.1. Rapid Acceleration Operation

First, the sensorless acceleration performance is evaluated in this section. Figures 11–14 compare two different drive accelerations when the position is estimated based on the PLL in Figure 4a,b. The acceleration rates are, respectively, 60 krpm/s (4 kHz/s) and 30 krpm/s (2 kHz/s). As explained in Section 3.3, degraded drive performance during the rapid drive acceleration might occur if the small-signal approximation in (16) is applied.

Figure 11 shows the acceleration of 60 krpm/s when the PLL in Figure 4a is implemented. Time-domain waveforms of $i_q(kT)$, $\hat{\omega}_e(kT)$, the normalized $-\hat{e}_{d_pu}(kT)$ and $\hat{\theta}_e(kT)$ are demonstrated. Similar to Figure 8, the normalized $\hat{e}_{d_pu}(kT)$ with only $\sin[\theta_{err}(kT)]$ is shown to enable easy comparison of the waveform with the signal from the arctangent calculation. It is shown that considerable oscillations on $\hat{e}_{d_pu}(kT)$ and $\hat{\omega}_e(kT)$ are observed under rapid acceleration. Due to the approximation error on $\sin[\theta_{err}(kT)]$, the oscillation from -1 rad to 1 rad results in $\hat{e}_{d_pu}(kT)$. The sensorless drive eventually fails at $\hat{\omega}_e(kT) = 21$ krpm and $f_{sample}/f_e = 7.14$ because of the positive PLL signal feedback once $\sin[\theta_{err}(kT)]$ reaches 1 rad. Contrarily, Figure 12 shows the same acceleration when the PLL in Figure 4b is implemented. Instead of $\hat{e}_{d_pu}(kT)$, the feedback signal of $\tan^{-1}[-\hat{e}_d(kT)/\hat{e}_q(kT)]$ in (17) is shown for comparison. By adding the arctangent calculation, the sensorless drive can successfully accelerate to 32 krpm at the acceleration rate of 60 krpm/s.

In addition, two sensorless drives under a low acceleration rate of 30 krpm/s are also evaluated in Figures 13 and 14. In Figure 13, the position and speed are estimated based on the PLL in Figure 4a, where the small-signal approximation is applied. By contrast, in Figure 14 the same acceleration for the sensorless drive with the PLL in Figure 4b is tested. It is demonstrated that two acceleration responses are almost the same at the acceleration rate of 30 krpm/s. Based on these experimental results, it is concluded that rapid acceleration performance is better for the sensorless drive using the proposed PLL estimation in Figure 4b, while the conventional PLL in Figure 4a results in a comparable performance when the acceleration rate is below 30 krpm/s.

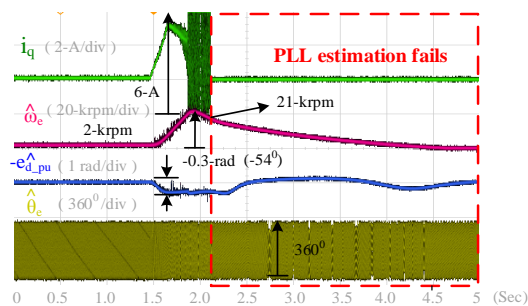


Figure 11. Machine acceleration from 2 krpm to 32 krpm ($f_{sample}/f_e = 5$) within 0.5 s based on the speed control where the PLL estimation with the feedback from \hat{e}_d is applied.

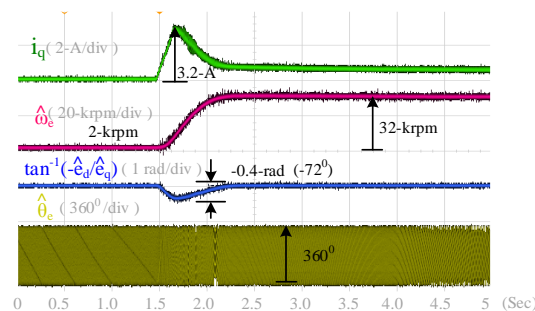


Figure 12. Machine acceleration from 2 krpm to 32 krpm ($f_{sample}/f_e = 5$) within 0.5 s based on the speed control where the PLL estimation with the arctangent calculation is implemented.

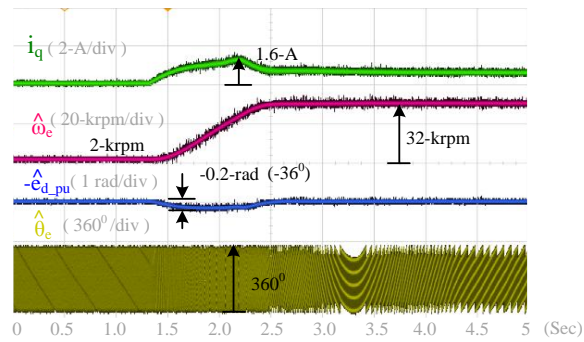


Figure 13. Machine acceleration from 2 krpm to 32 krpm ($f_{sample}/f_e = 5$) within 1 s based on the speed control where the PLL estimation with the feedback from \hat{e}_d is applied.

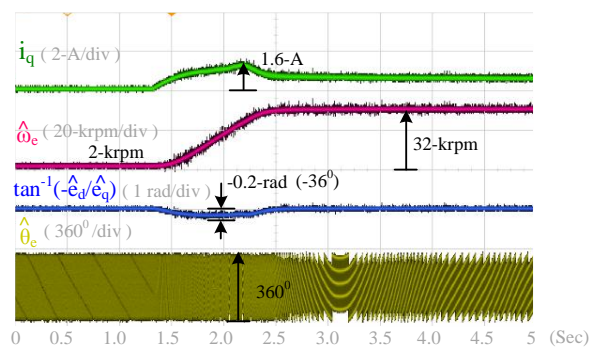


Figure 14. Machine acceleration from 2 krpm to 32 krpm ($f_{sample}/f_e = 5$) within 1 s based on the speed control where the PLL estimation with the arctangent calculation is implemented.

4.2. Dynamic Load Operation:

This section evaluates the sensorless speed closed-loop control performance under a 100% step load at 12 krpm ($f_{sample}/f_e = 12.5$). In Figure 15, the position is estimated based on the PLL with feedback from $\hat{e}_d(kT)$. Time-domain signals of $i_q(kT)$, $i_d(kT)$, $\hat{e}_{d_pu}(kT)$ and $\hat{\omega}_e(kT)$, respectively, are shown. A visible oscillation on $\hat{e}_{d_pu}(kT)$ and $\hat{\omega}_e(kT)$ occurs when a 100% step load is suddenly applied. Similar to the prior acceleration test, the approximation in (16) is the primary issue for degraded sensorless drive performance. Although this oscillation eventually decreases to zero at a steady state, the dynamic operation is limited, especially at high speed. It is also noted that it is not possible to maintain the stability of the sensorless drive using the same PLL estimation when the step load is beyond 100%.

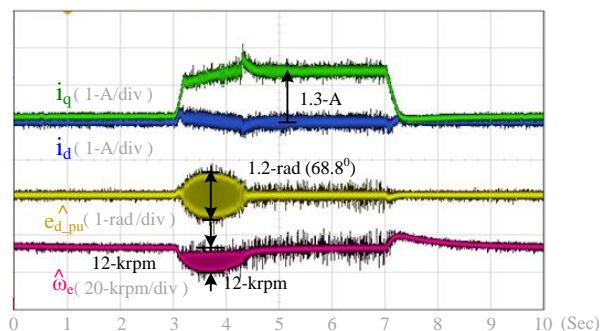


Figure 15. Sensorless speed control under a step load at 12 krpm ($f_{sample}/f_e = 12.5$) when the PLL estimation with the feedback from \hat{e}_d is applied.

Figure 16 shows the same speed control performance under a 100% step load. In this experiment, $\tan^{-1}[-\hat{e}_d(kT)/\hat{e}_q(kT)]$ instead of $\hat{e}_d(kT)$ is applied for the PLL estimation. Time-domain signals of $i_q(kT)$, $i_d(kT)$, $\tan^{-1}[-\hat{e}_d(kT)/\hat{e}_q(kT)]$ and $\hat{\omega}_e(kT)$ are illustrated. By using actual $\theta_{err}(kT)$ for the PLL estimation, the transient oscillation on $\hat{\omega}_e(kT)$ is resolved, resulting in improved dynamic performance. Similar to the acceleration experiment at 4.1, the performance of the sensorless drive under the step load is also better using the proposed PLL estimation with $\tan^{-1}[-\hat{e}_d(kT)/\hat{e}_q(kT)]$. The D-axis current signal is a key performance indicator for evaluating the sensorless drive performance. For SPM machines, $i_d(kT)$ should be controlled so as to maintain it at zero. As seen for the load transient in Figure 16 when $t = 3\sim 4$ s, $i_d(kT)$ achieves negligible fluctuation. By contrast, in Figure 15 the waveform distortion of $i_d(kT)$ is observed, leading to degraded drive performance.

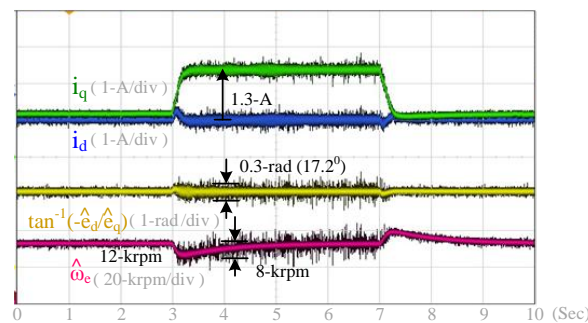


Figure 16. Sensorless speed control under a step load at 12 krpm ($f_{sample}/f_e = 12.5$) when the PLL estimation with the arctangent calculation is implemented.

4.3. Parameter Sensitivity

This section evaluates the sensorless speed closed-loop control performance considering parameter estimation errors. The influences of both resistance and inductance estimation error on the sensorless drive are evaluated.

Figure 17 shows the sensorless speed closed-loop control at 12 krpm ($f_{sample}/f_e = 12.5$) when the resistance error is considered. In order to clearly evaluate the drive performance with respect to the resistance error, \hat{R}_s is continuously changed from $0.5R_s$ to $2R_s$ during the speed closed-loop control. In (a), the PLL estimation with the feedback from $-\hat{e}_d(kT)$ is implemented. On the other hand, the PLL estimation with the actual $\theta_{err}(kT)$ from the arctangent calculation is implemented in (b). Time-domain waveforms of $i_q(kT)$, $\hat{\omega}_e(kT)$, $\hat{e}_{d_pu}(kT)$ or $\tan^{-1}[-\hat{e}_d(kT)/\hat{e}_q(kT)]$ and ΔR_s , respectively, are demonstrated. Due to the relatively low resistive voltage drop at high speed, the resistance error seems to be insensitive to the sensorless drive for the PLL estimation with the feedback signal either from $-\hat{e}_d(kT)$ in Figure 17a and $\tan^{-1}[-\hat{e}_d(kT)/\hat{e}_q(kT)]$ in Figure 17b.

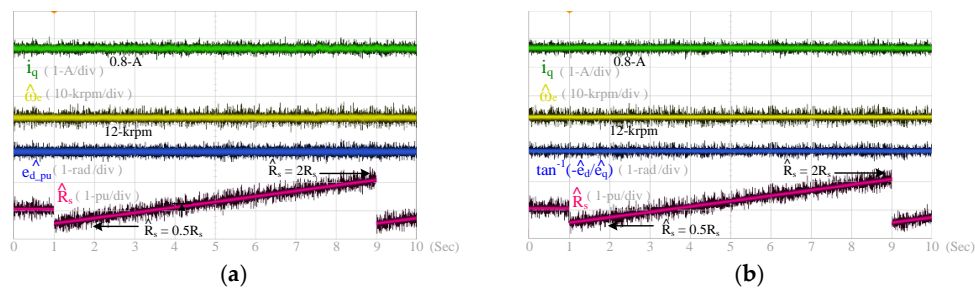


Figure 17. Constant speed closed-loop control at 12 krpm ($f_{sample}/f_e = 12.5$) with the resistance estimation error when the PLL estimation is implemented with the feedback from (a) \hat{e}_d and (b) arctangent.

Similar to the experiment on the resistance error, Figure 18 shows the same speed closed-loop control at 12 krpm ($f_{sample}/f_e = 12.5$) while the inductance error is considered. In this experiment, \hat{L}_s is changed from $0.5L_s$ to $2L_s$ during the closed-loop control. The PLL estimation with the feedback from $\hat{e}_d(kT)$ and $\tan^{-1}[-\hat{e}_d(kT)/\hat{e}_q(kT)]$ are applied in (a) and (b), respectively. Because the inductive voltage drop is proportional to the operating speed, the small inductance variation results in the considerable position estimation error on the drive at high speed. As seen in Figure 18a, the speed control eventually fails with $\hat{L}_s = 1.2L_s$ at 12 rpm if $-\hat{e}_d(kT)$ is directly used for the position and speed estimation. The use of only d-axis EMF voltage for the PLL regulation is the primary factor causing this stability issue. In general, inductance should decrease at high speed due to the skin effect. Thus, the conventional PLL estimation in Figure 4a might not be suited for the sensorless drive at high speed. On the contrary, in Figure 18b the speed control maintains at 12 krpm even when the inductance error is $\hat{L}_s = 2L_s$. By applying both d- and q-axis EMF voltages for the PLL estimation in Figure 4b, it is concluded that the reduced effect of the inductance error on the high-speed sensorless drive can be achieved.

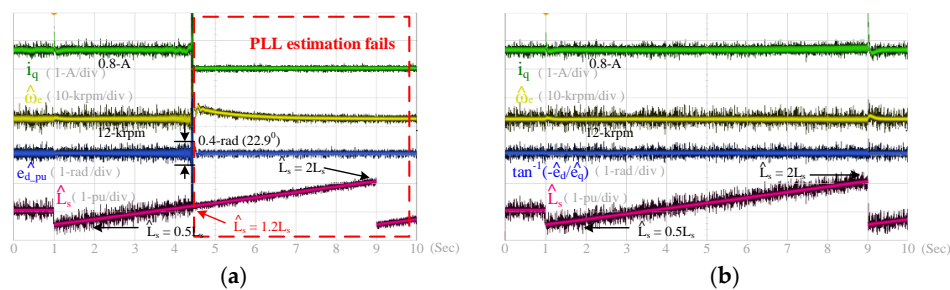


Figure 18. Constant speed closed-loop control at 12 krpm ($f_{sample}/f_e = 12.5$) with the inductance estimation error when the PLL estimation is implemented with the feedback from (a) \hat{e}_d and (b) arctangent.

4.4. 36-krpm Sensorless Drive under Load

Figure 19 shows the sensorless closed-loop control performance under 50% step load, where the speed is maintained at 36 krpm ($f_e = 2.4$ -kHz and $f_{pwm}/f_e = 4.2$). In this test, the position and speed is estimated based on the PLL in Figure 4b with the feedback from $\tan^{-1}[-\hat{e}_d(kT)/\hat{e}_q(kT)]$. By applying the proposed PLL estimation, the sensorless drive can maintain the closed-loop control with only 4.2 sampling points per electric cycle. In addition, (b) and (c) illustrate zoom-in waveforms at no load and 50% load respectively. It is concluded that A-phase current, i_a measured by the current probe, can be regulated to maintain the sinusoidal waveform, resulting in improved drive performance at high speed.

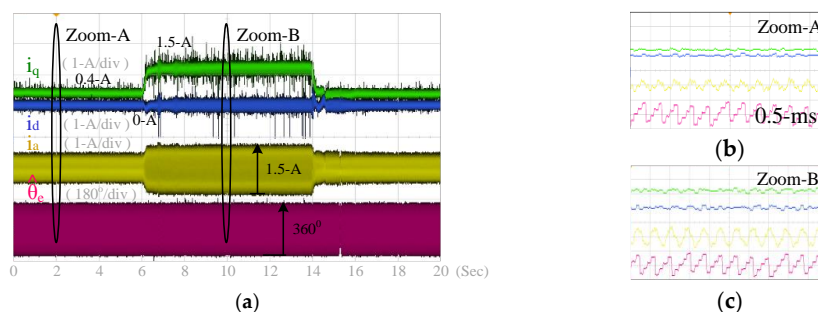


Figure 19. (a) Sensorless speed closed-loop control at $\omega_e = 2\pi \times 2.4$ kHz and $f_{sample}/f_e = 4.2$ with 50% step load when the PLL estimation in Figure 4b is applied. The no-load and 50%-load waveforms are zoomed in on at (b) and (c).

4.5. Sensorless Drive at Low Speed

Figures 20 and 21 compare the sensorless speed closed-loop control using two different PLL estimations at the speed of 1.5 krpm (12.5% rated speed). In these tests, a 100% step load is applied while the speed is controlled to be maintained at 1.5 krpm. In Figure 20, the position and speed are all estimated based on the conventional PLL in Figure 4a with the feedback from \hat{e}_d . By contrast, in Figure 21 the proposed PLL in Figure 4b is applied by cascading the arctangent calculation. The speed controller bandwidths are all designed at 10 Hz. By comparing the results in Figures 20 and 21, it is concluded that the two estimation methods achieve a similar closed-loop control performance when the sensorless drive is operated in the low-speed region.

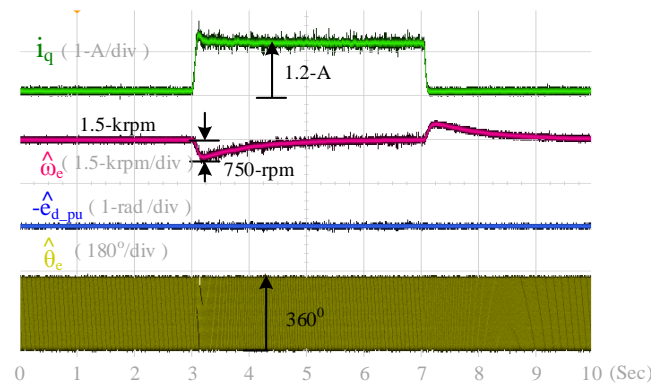


Figure 20. Sensorless speed control under a 100% step load at 1.5 krpm (12.5% rated speed) when the PLL estimation with the feedback from \hat{e}_d is applied.

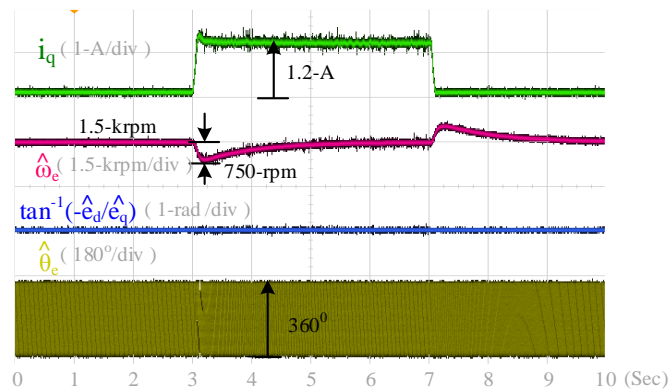


Figure 21. Sensorless speed control under a 100% step load at 1.5 krpm (12.5% rated speed) when the PLL estimation with the arctangent calculation is implemented.

5. Conclusions

This paper improves sensorless position estimation at high speed. Compared to conventional small-signal approximation, the proposed PLL shows better performance in estimating position, especially at high speed with a low ratio of f_{sample}/f_e . By using the discrete-time EMF estimation and proposed PLL, the FOC drive can be maintained at the speed of 36 krpm under 50% step torque load, with only 4.2 sampling points in an electrical cycle.

Acknowledgments: The authors gratefully acknowledge the financial support of the National Science Council of Taiwan, R.O.C. through its grants 106-2628-E-002-014-MY3.

Author Contributions: Guan-Ren Chen and Shih-Chin Yang wrote the paper. Shih-Chin Yang developed sensorless drive algorithms. Guan-Ren Chen implemented and verified all the theories and performed all the experiments. Yu-Liang Hsu and Kang Li contributed analysis tools.

Conflicts of Interest: The authors declare no conflict of interest.

References

1. Gerada, D.; Mebarki, A.; Brown, N.L.; Gerada, C.; Cavagnino, A.; Boglietti, A. High-Speed Electrical Machines: Technologies, Trends, and Developments. *IEEE Trans. Ind. Electron.* **2014**, *61*, 2946–2959. [[CrossRef](#)]
2. Van der Geest, M.; Polinder, H.; Ferreira, J.A.; Christmann, M. Power Density Limits and Design Trends of High-Speed Permanent Magnet Synchronous Machines. *IEEE Trans. Transp. Electrification* **2015**, *1*, 266–276. [[CrossRef](#)]
3. Guagnano, A.; Rizzello, G.; Cupertino, F.; Naso, D. Robust Control of High-Speed Synchronous Reluctance Machines. *IEEE Trans. Ind. Appl.* **2016**, *52*, 3990–4000. [[CrossRef](#)]
4. Bon-Ho, B.; Seung-Ki, S. A compensation method for time delay of full-digital synchronous frame current regulator of pwm ac drives. *IEEE Trans. Ind. Appl.* **2003**, *39*, 802–810. [[CrossRef](#)]
5. Zwysig, C.; Kolar, J.W.; Round, S.D. Megaspeed Drive Systems: Pushing Beyond 1 Million r/min. *IEEE/ASME Trans. Mechatron.* **2009**, *14*, 564–574. [[CrossRef](#)]
6. Bon-Ho, B.; Seung-Ki, S.; Jeong-Hyeck, K.; Ji-Seob, B. Implementation of sensorless vector control for super-high-speed pmsm of turbo-compressor. *IEEE Trans. Ind. Appl.* **2003**, *39*, 811–818. [[CrossRef](#)]
7. Yan, H.; Xu, Y.; Zou, J. A Phase Current Reconstruction Approach for Three-Phase Permanent-Magnet Synchronous Motor Drive. *Energies* **2016**, *9*, 853. [[CrossRef](#)]
8. Gamazo-Real, J.C.; Vázquez-Sánchez, E.; Gómez-Gil, J. Position and Speed Control of Brushless DC Motors Using Sensorless Techniques and Application Trends. *Sensors* **2010**, *10*, 6901–6947. [[CrossRef](#)] [[PubMed](#)]
9. Harnefors, L.; Nee, H.P. A general algorithm for speed and position estimation of AC motors. *IEEE Trans. Ind. Electron.* **2000**, *47*, 77–83. [[CrossRef](#)]
10. Fengxiang, W.; Zhe, C.; Stolze, P.; Stumper, J.-F.; Rodriguez, J.; Kennel, R. Encoderless Finite-State Predictive Torque Control for Induction Machine With a Compensated MRAS. *IEEE Trans. Ind. Inf.* **2014**, *10*, 1097–1106. [[CrossRef](#)]
11. Jansen, P.L.; Lorenz, R.D. Transducerless position and velocity estimation in induction and salient AC machines. *IEEE Trans. Ind. Appl.* **1995**, *31*, 240–247. [[CrossRef](#)]
12. Young-Doo, Y.; Seung-Ki, S.; Morimoto, S.; Ide, K. High-Bandwidth Sensorless Algorithm for AC Machines Based on Square-Wave-Type Voltage Injection. *IEEE Trans. Ind. Appl.* **2011**, *47*, 1361–1370. [[CrossRef](#)]
13. Hejny, R.W.; Lorenz, R.D. Evaluating the Practical Low-Speed Limits for Back-EMF Tracking-Based Sensorless Speed Control Using Drive Stiffness as a Key Metric. *IEEE Trans. Ind. Appl.* **2011**, *47*, 1337–1343. [[CrossRef](#)]
14. Matsui, N. Sensorless PM brushless DC motor drives. *IEEE Trans. Ind. Electron.* **1996**, *43*, 300–308. [[CrossRef](#)]
15. Bernardes, T.; Montagner, V.F.; Grudling, H.A.; Pinheiro, H. Discrete-Time Sliding Mode Observer for Sensorless Vector Control of Permanent Magnet Synchronous Machine. *IEEE Trans. Ind. Electron.* **2014**, *61*, 1679–1691. [[CrossRef](#)]
16. Nguyen, D.; Dutta, R.; Rahman, M.F.; Fletcher, J.E. Performance of a Sensorless Controlled Concentrated-Wound Interior Permanent-Magnet Synchronous Machine at Low and Zero Speed. *IEEE Trans. Ind. Electron.* **2016**, *63*, 2016–2026. [[CrossRef](#)]
17. Wu, X.; Wang, H.; Huang, S.; Huang, K.; Wang, L. Sensorless Speed Control with Initial Rotor Position Estimation for Surface Mounted Permanent Magnet Synchronous Motor Drive in Electric Vehicles. *Energies* **2015**, *8*, 11030–11046. [[CrossRef](#)]
18. Jung, T.-U.; Jang, J.-H.; Park, C.-S. A Back-EMF Estimation Error Compensation Method for Accurate Rotor Position Estimation of Surface Mounted Permanent Magnet Synchronous Motors. *Energies* **2017**, *10*, 1160. [[CrossRef](#)]
19. Corley, M.J.; Lorenz, R.D. Rotor position and velocity estimation for a salient-pole permanent magnet synchronous machine at standstill and high speeds. *IEEE Trans. Ind. Appl.* **1998**, *34*, 784–789. [[CrossRef](#)]
20. Tian, L.; Zhao, J.; Sun, J. Sensorless Control of Interior Permanent Magnet Synchronous Motor in Low-Speed Region Using Novel Adaptive Filter. *Energies* **2016**, *9*, 1084. [[CrossRef](#)]
21. Shen, J.X.; Zhu, Z.Q.; Howe, D. Improved speed estimation in sensorless PM brushless AC drives. *IEEE Trans. Ind. Appl.* **2002**, *38*, 1072–1080. [[CrossRef](#)]

22. Suzuki, T.; Shimizu, Y.; Iwaji, Y.; Takahata, R.; Aoyagi, S. Minimum Current Start-Up Method by Combined Use of Two Position-Sensorless Controls. *IEEE Trans. Ind. Appl.* **2015**, *51*, 3086–3093. [[CrossRef](#)]
23. Tatemarsu, K.; Hamada, D.; Uchida, K.; Wakao, S.; Onuki, T. New approaches with sensorless drives. *IEEE Ind. Appl. Mag.* **2000**, *6*, 44–50. [[CrossRef](#)]
24. Wallmark, O.; Harnefors, L.; Carlson, O. An Improved Speed and Position Estimator for Salient Permanent-Magnet Synchronous Motors. *IEEE Trans. Ind. Electron.* **2005**, *52*, 255–262. [[CrossRef](#)]
25. Wallmark, O.; Harnefors, L. Sensorless Control of Salient PMSM Drives in the Transition Region. *IEEE Trans. Ind. Electron.* **2006**, *53*, 1179–1187. [[CrossRef](#)]
26. Kim, H.; Harke, M.C.; Lorenz, R.D. Sensorless control of interior permanent-magnet machine drives with zero-phase lag position estimation. *IEEE Trans. Ind. Appl.* **2003**, *39*, 1726–1733.
27. Chi, S.; Zhang, Z.; Xu, L.Y. Sliding-Mode Sensorless Control of Direct-Drive PM Synchronous Motors for Washing Machine Applications. *IEEE Trans. Ind. Appl.* **2009**, *45*, 582–590. [[CrossRef](#)]
28. Morimoto, S.; Kawamoto, K.; Sanada, M.; Takeda, Y. Sensorless control strategy for salient-pole PMSM based on extended EMF in rotating reference frame. *IEEE Trans. Ind. Appl.* **2002**, *38*, 1054–1061. [[CrossRef](#)]
29. Yim, J.S.; Sul, S.K.; Bae, B.T.; Patel, N.R.; Hiti, S. Modified Current Control Schemes for High-Performance Permanent-Magnet AC Drives With Low Sampling to Operating Frequency Ratio. *IEEE Trans. Ind. Appl.* **2009**, *45*, 763–771. [[CrossRef](#)]
30. Bolognani, S.; Tubiana, L.; Zigliotto, M. Extended kalman filter tuning in sensorless PMSM drives. *IEEE Trans. Ind. Appl.* **2003**, *39*, 1741–1747. [[CrossRef](#)]
31. Bolognani, S.; Zigliotto, M.; Zordan, M. Extended-range PMSM sensorless speed drive based on stochastic filtering. *IEEE Trans. Power Electron.* **2001**, *16*, 110–117. [[CrossRef](#)]
32. Guchuan, Z.; Kaddouri, A.; Dessaint, L.A.; Akhrif, O. A nonlinear state observer for the sensorless control of a permanent-magnet AC machine. *IEEE Trans. Ind. Electron.* **2001**, *48*, 1098–1108. [[CrossRef](#)]
33. Wang, T.C.; Lall, S.; Chiou, T.Y. Polynomial method for PLL controller optimization. *Sensors* **2011**, *11*, 6575–6592. [[CrossRef](#)] [[PubMed](#)]
34. Cho, Y. Improved Sensorless Control of Interior Permanent Magnet Sensorless Motors Using an Active Damping Control Strategy. *Energies* **2016**, *9*, 135. [[CrossRef](#)]
35. Yang, D.; Mok, H.; Lee, J.; Han, S. Adaptive Torque Estimation for an IPMSM with Cross-Coupling and Parameter Variations. *Energies* **2017**, *10*, 167. [[CrossRef](#)]
36. Awan, H.A.A.; Tuovinen, T.; Saarakkala, S.E.; Hinkkanen, M. Discrete-Time Observer Design for Sensorless Synchronous Motor Drives. *IEEE Trans. Ind. Appl.* **2016**, *52*, 3968–3979. [[CrossRef](#)]
37. Yang, S.-C.; Chen, G.-R. High-Speed Position-Sensorless Drive of Permanent-Magnet Machine Using Discrete-Time EMF Estimation. *IEEE Trans. Ind. Electron.* **2017**, *64*, 4444–4453. [[CrossRef](#)]
38. Bolognani, S.; Calligaro, S.; Petrella, R. Design Issues and Estimation Errors Analysis of Back-EMF-Based Position and Speed Observer for SPM Synchronous Motors. *IEEE J. Emerg. Select. Top. Power Electron.* **2014**, *2*, 159–170. [[CrossRef](#)]

